Computational Mechanics 26 (2000) 398–408 © Springer-Verlag 2000

An efficient meshless method for fracture analysis of cracks

B. N. Rao, S. Rahman

Abstract This paper presents an efficient meshless method for analyzing linear-elastic cracked structures subject to single- or mixed-mode loading conditions. The method involves an element-free Galerkin formulation in conjunction with an exact implementation of essential boundary conditions and a new weight function. The proposed method eliminates the shortcomings of Lagrange multipliers typically used in element-free Galerkin formulations. Numerical examples show that the proposed method yields accurate estimates of stress-intensity factors and near-tip stress field in two-dimensional cracked structures. Since the method is meshless and no element connectivity data are needed, the burdensome remeshing required by finite element method (FEM) is avoided. By sidestepping remeshing requirement, crack-propagation analysis can be dramatically simplified. Example problems on mixed-mode condition are presented to simulate crack propagation. The predicted crack trajectories by the proposed meshless method are in excellent agreement with the FEM or the experimental data.

1 Introduction

For many structures, crack propagation is an important failure mechanism requiring accurate numerical models to implement simulations essential for failure prediction. To perform numerical simulation, the computational methods must be applied to determine fracture response and reliability of cracked structures. A current popular method is the finite element method (FEM), which has been extensively used for fracture analysis of cracks. Although a significant amount of the research in FEM is useful, the method has serious limitations in solving solid mechanics problems characterized by a continuous change in geometry of the domain under analysis. Crack propagation is a prime example in which the use of FEM requires a large number of remeshings of the finite element model to represent arbitrary and complex paths. The underlying structures of FEM and similar methods, which rely on a mesh, is quite cumbersome in treating cracks that are not coincident with the original mesh geometry. Consequently, the only viable option for dealing with moving cracks using the FEM is to remesh during each discrete step of model evolution so that mesh lines remain coincident with cracks throughout the analysis. This creates numerical difficulties, often leading to degradation of solution accuracy, complexity in computer programming, and a computationally intensive environment.

In recent years, a class of meshfree or meshless methods, such as smooth particle hydrodynamics [1–3], diffuse element method [4], element-free Galerkin method (EFGM) [5–7], h–p clouds [8], partition of unity [9], reproducing kernel particle method [10–11], meshless local Petrov–Galerkin method [12], and local boundary integral equation method [13], appear to demonstrate significant potential for the moving boundary problem typified by growing cracks. Fundamental to all meshless methods, a structured mesh is not used, since only a scattered set of nodal points is required in the domain of interest. This feature presents significant implications for modeling fracture propagation, because the domain of interest is completely discretized by a set of nodes. Since no element connectivity data are needed, the burdensome remeshing required by FEM is avoided. A growing crack can be modeled by simply extending the free surfaces, which correspond to the crack. By sidestepping remeshing requirements, crack-propagation analysis can be dramatically simplified.

For fracture analysis of cracks, the EFGM is the first meshless method introduced by Belytschko and his coworkers [5–7]. In the original EFGM [5–7], the meshless shape functions do not represent interpolation functions. Hence, the essential boundary conditions cannot be imposed exactly due to loss of Kronecker-delta properties. Initially, Belytschko et al. [5] employed the general Lagrange multipliers approach to impose the boundary conditions. This requires solution of the Lagrange multipliers in addition to the discrete field variables. This leads to a larger size of the system matrix, loss of the bandedness of the system matrix, and an awkward linear equation structure. The matrix, which has to be inverted, possesses zeroes in the diagonal elements and thus may require special solvers that cannot utilize the positive-definiteness of the system matrix. Subsequently, Lu et al. [6] proposed a modified variational principle in which Lagrange

Received 6 March 2000

B. N. Rao, S. Rahman (✉)
College of Engineering, The University of Iowa,
Iowa City, IA 52242, USA

The authors would like to acknowledge the financial support by the U.S. National Science Foundation (Grant No. CMS-9900196). Dr. Ashland Brown was the Program Director. The authors would also like to thank Professor J.S. Chen at The University of Iowa for his encouragement and guidance for working in the field of meshless method.

multipliers are replaced by their physical meaning. Although this leads to banded set of equations, (but not necessarily positive-definite matrices), the results are not as accurate when compared with those by the Lagrange multipliers approach. Another approach proposed by Krongauz and Belytschko [14] is to necklace the EFGM domain with the FEM domain and apply the boundary conditions to the finite element nodes. This coupling technique dramatically simplifies the enforcement of boundary conditions, but compromises the salient features of EFGM. In a recent work, Kaljevic and Saigal [15] introduced a singular weight function into the moving least-squares approximation to reproduce the Kronecker-delta properties. This technique thus allows the enforcement of essential boundary conditions more efficiently. For applications other than fracture, methods based on penalty functions [16] and alternative definitions of discrete norm [17] have also been reported. Indeed, there is a considerable interest in exploring methods to improve the imposition of essential boundary conditions in EFGM or other meshless methods.

This paper presents an efficient formulation of the EFGM for fracture analysis of cracks in homogenous, isotropic, linear-elastic two-dimensional solids. The proposed method involves enforcement of essential boundary conditions by a transformation method and a new weight function. Both single- (mode I) and mixed-mode (modes I and II) problems can be solved by this method. A number of examples are presented to evaluate the accuracy of stress-intensity factors (SIFs) calculated by this method. Furthermore, this method was applied to model crack propagation under mixed-mode loading condition. Comparisons were made between the crack trajectories predicted by the proposed meshless method with the FEM and the experiment.

2 Moving least-squares approximation

Consider a function, $u(\mathbf{x})$ over a domain, $\Omega \subseteq \Re^K$, where $K = 1, 2$, or 3. Let $\Omega_x \subseteq \Omega$ denote a sub-domain describing the neighborhood of a point, $\mathbf{x} \in \Re^K$ located in Ω. According to the moving least-squares (MLS) [18], the approximation, $u^h(\mathbf{x})$ of $u(\mathbf{x})$ is

$$u^h(\mathbf{x}) = \sum_{i=1}^{m} p_i(\mathbf{x}) a_i(\mathbf{x}) = \mathbf{p}^{\mathrm{T}}(\mathbf{x})\mathbf{a}(\mathbf{x}) \tag{1}$$

where $\mathbf{p}^{\mathrm{T}}(\mathbf{x}) = \{p_1(\mathbf{x}), p_2(\mathbf{x}), \ldots, p_m(\mathbf{x})\}$ is a vector of complete basis functions of order m and $\mathbf{a}(\mathbf{x}) = \{a_1(\mathbf{x}), a_2(\mathbf{x}), \ldots, a_m(\mathbf{x})\}$ is a vector of unknown parameters that depend on $\mathbf{x}$. The basis functions should satisfy the following properties: (1) $p_1(\mathbf{x}) = 1$, (2) $p_i(\mathbf{x}) \in C^s(\Omega)$, $i = 1, 2, \ldots, m$ where $C^s(\Omega)$ is a set of functions that have continuous derivatives up to order s on Ω, and (3) $p_i(\mathbf{x}), i = 1, 2, \ldots, m$ constitute a linearly independent set. For example, in two dimensions ($K = 2$) with x_1- and x_2-coordinates

$$\mathbf{p}^{\mathrm{T}}(\mathbf{x}) = \{1, x_1, x_2\}, \ m = 3 \tag{2}$$

and

$$\mathbf{p}^{\mathrm{T}}(\mathbf{x}) = \{1, x_1, x_2, x_1^2, x_1x_2, x_2^2\}, \ m = 6 \tag{3}$$

representing linear and quadratic basis functions, respectively. These basis functions are not required to be polynomials as shown in Eqs. (2) and (3). When solving problems involving cracks, a convenient way of capturing $1/\sqrt{r}$ stress-singularity in linear-elastic fracture mechanics (LEFM) is by using [19]

$$\mathbf{p}^{\mathrm{T}}(x) = \{1, x_1, x_2, \sqrt{r}\}, \ m = 4 \tag{4}$$

or

$$\mathbf{p}^{\mathrm{T}}(x) = \{1, x_1, x_2, \sqrt{r}\cos(\theta/2), \sqrt{r}\sin(\theta/2), \sqrt{r}\sin(\theta/2)\sin\theta, \sqrt{r}\cos(\theta/2)\sin\theta\}, \ m = 7 \tag{5}$$

where r and θ are polar coordinates with the crack tip as the origin. Equations (4) and (5) represent radially (partially) enriched and fully enriched basis functions, respectively.

In Eq. (1), the coefficient vector, $\mathbf{a}(\mathbf{x})$ is determined by minimizing a weighted discrete $\mathscr{L}_2$ norm, defined as

$$\begin{aligned} J(\mathbf{x}) &= \sum_{I=1}^{n} w_I(\mathbf{x})[\mathbf{p}^{\mathrm{T}}(\mathbf{x}_I)\mathbf{a}(\mathbf{x}) - d_I]^2 \\ &= [\mathbf{P}\mathbf{a}(\mathbf{x}) - \mathbf{d}]^{\mathrm{T}}\mathbf{W}[\mathbf{P}\mathbf{a}(\mathbf{x}) - \mathbf{d}] \end{aligned} \tag{6}$$

where $\mathbf{x}_I$ denotes the coordinates of node I, $\mathbf{d}^{\mathrm{T}} = \{d_1, d_2, \ldots, d_n\}$ with d_I representing the nodal parameter (not the nodal values of $u^h(\mathbf{x})$) for node I, $\mathbf{W} = \mathrm{diag}[w_1(\mathbf{x}), w_2(\mathbf{x}), \ldots, w_N(\mathbf{x})]$ with $w_I(\mathbf{x})$ denoting the weight function associated with node I such that $w_I(\mathbf{x}) \geq 0$ for all $\mathbf{x}$ in the support Ω_x of $w_I(\mathbf{x})$ and zero otherwise, n is the number of nodes in Ω_x for which $w_I(\mathbf{x}) > 0$, and

$$\mathbf{P} = \begin{bmatrix} \mathbf{p}^{\mathrm{T}}(\mathbf{x}_1) \\ \mathbf{p}^{\mathrm{T}}(\mathbf{x}_2) \\ \vdots \\ \mathbf{p}^{\mathrm{T}}(\mathbf{x}_n) \end{bmatrix} \in \mathscr{L}(\Re^n \times \Re^m) \ . \tag{7}$$

The stationarity of $J(\mathbf{x})$ with respect to $\mathbf{a}(\mathbf{x})$ yields

$$\mathbf{A}(\mathbf{x})\mathbf{a}(\mathbf{x}) = \mathbf{C}(\mathbf{x})\mathbf{d} \tag{8}$$

where

$$\mathbf{A}(\mathbf{x}) = \sum_{I=1}^{n} w_I(\mathbf{x})\mathbf{p}(\mathbf{x}_I)\mathbf{p}^{\mathrm{T}}(\mathbf{x}_I) = \mathbf{P}^{\mathrm{T}}\mathbf{W}\mathbf{P} \tag{9}$$

$$\mathbf{C}(\mathbf{x}) = [w_1(\mathbf{x})\mathbf{p}(\mathbf{x}_1), \ldots, w_n(\mathbf{x})\mathbf{p}(\mathbf{x}_n)] = \mathbf{P}^{\mathrm{T}}\mathbf{W} \tag{10}$$

Solving $\mathbf{a}(\mathbf{x})$ from Eq. (8) and then substituting it in Eq. (1) gives

$$u^h(\mathbf{x}) = \sum_{I=1}^{n} \Phi_I(\mathbf{x}) d_I = \mathbf{\Phi}^{\mathrm{T}}(\mathbf{x})\mathbf{d} \tag{11}$$

where

$$\begin{aligned} \mathbf{\Phi}^{\mathrm{T}}(\mathbf{x}) &= \{\Phi_1(\mathbf{x}), \Phi_2(\mathbf{x}), \ldots, \Phi_n(\mathbf{x})\} \\ &= \mathbf{p}^{\mathrm{T}}(\mathbf{x})\mathbf{A}^{-1}(\mathbf{x})\mathbf{C}(\mathbf{x}) \end{aligned} \tag{12}$$

is a vector with its Ith component

$$\Phi_I(\mathbf{x}) = \sum_{j=1}^{m} p_j(\mathbf{x})[\mathbf{A}^{-1}(\mathbf{x})\mathbf{C}(\mathbf{x})]_{jI} \tag{13}$$

representing the shape function of the MLS approximation corresponding to node I. The partial derivatives of $\Phi_I(\mathbf{x})$ can be obtained as follows:

$$\Phi_{I,i}(\mathbf{x}) = \sum_{j=1}^{m} \left\{ p_{j,i}(\mathbf{A}^{-1}\mathbf{C})_{jI} + p_j(\mathbf{A}_{,i}^{-1}\mathbf{C} + \mathbf{A}^{-1}\mathbf{C}_{,i})_{jI} \right\} \tag{14}$$

where

$$\mathbf{A}_{,i}^{-1} = -\mathbf{A}^{-1}\mathbf{A}_{,i}\mathbf{A}^{-1} \tag{15}$$

in which $(\,)_{,i} = \partial(\,)/\partial x_i$.

Note, the MLS shape function, $\Phi_I(\mathbf{x})$ strongly depends on the type of basis functions used. For problem involving cracks, the enriched basis functions, given by Eqs. (4) or (5), are required to produce stress singularity at the crack tip. However, this singularity field is only local to the crack tip. Therefore, it is unnecessary to use enriched basis for the entire domain. In that case, a hybrid approach involving enriched basis close to the crack tip and regular basis far away from the crack tip can be used. For example, if $\Phi_I^r(x)$ and $\Phi_I^e(x)$ denote two resulting shape functions using regular (e.g., Eqs. (2) or (3)) and enriched (e.g., Eqs. (4) or (5)) basis functions, respectively, the effective shape function due to coupling can be expressed by [19]

$$\Phi_I(\mathbf{x}) = R\Phi_I^e(\mathbf{x}) + (1-R)\Phi_I^r(\mathbf{x}) \tag{16}$$

where R is an appropriate ramp functions that is equal to unity on the enriched boundary of the coupling region and zero on the regular side of the coupling region.

3 Weight function

An important ingredient of EFGM or other meshless methods is the weight function, $w(\mathbf{x})$. The choice of the weight function can affect the MLS approximation of $u^h(\mathbf{x})$. In this work, a new weight function based on the Student's t-distribution is proposed. It is given by

$$w_I(\mathbf{x}) = \begin{cases} \dfrac{\left(1+\beta^2(z_I^2/z_{mI}^2)\right)^{-((1+\beta)/2)} - (1+\beta^2)^{-((1+\beta)/2)}}{1-\left(1+\beta^2\right)^{-((1+\beta)/2)}}, & z_I \le z_{mI} \\ 0, & z_I > z_{mI} \end{cases} \tag{17}$$

where β is the parameter controlling the shape of the weight function, $z_I = \|\mathbf{x} - \mathbf{x}_I\|$ is the distance from a sampling point, $\mathbf{x}$ to a node $\mathbf{x}_I$, z_{mI} is the domain of influence of node I such that

$$z_{mI} = z_{\max} z_{cI} \tag{18}$$

in which z_{cI} is a the characteristic nodal spacing distance which is chosen such that the node I has enough number of neighbors sufficient for regularity of $\mathbf{A}(\mathbf{x})$ in Eq. (9) (which is used to determine the MLS approximation), and $z_{\max}$ is a scaling parameter. Note, the t-distribution used in Eq. (17) represents the probability density function of a standard Gaussian random variable divided by the square root of a χ^2 random variable with β degrees of freedom [20].

The smoothness of the shape functions, $\Phi_I(\mathbf{x})$ is governed by the smoothness of the weight function and basis functions. If $p_i(\mathbf{x}) \in C^s(\Omega)$ and $w_I(\mathbf{x}) \in C^r(\Omega)$, then it can be shown that $\Phi_I(\mathbf{x}) \in C^{\min(r,s)}(\Omega)$. To avoid poorly formed shape functions, $w_I(\mathbf{x})$ should be unity at the center and zero along the boundary of Ω_x. Also, appropriate values of β depending on the basis function should be selected.

To avoid any discontinuities in the shape functions due to the presence of cracks, a diffraction method [19, 21] can be used to modify z_I in the weight function. According to this method, when the line joining the node x_I to the sampling point $\mathbf{x}$ intersects the crack segment and the crack tip is within the domain of influence of the node x_I, z_I is modified as [19]

$$z_I = \left(\frac{s_1 + s_2(\mathbf{x})}{s_0(\mathbf{x})}\right)^{\lambda} s_0(\mathbf{x}) \tag{19}$$

where $s_1 = \|\mathbf{x}_I - \mathbf{x}_c\|$, $s_2(\mathbf{x}) = \|\mathbf{x} - \mathbf{x}_c\|$, $s_0(\mathbf{x}) = \|\mathbf{x} - \mathbf{x}_I\|$, $\mathbf{x}$ and $\mathbf{x}_c$ are the coordinates of the sampling point and crack tip, respectively, and $1 \le \lambda \le 2$ is a parameter for adjusting the distance of the support on the opposite side of the crack.

4 Variational formulation and discretization

For small displacements in two-dimensional, homogeneous, isotropic, and linear-elastic solids, the equilibrium equations and boundary conditions are

$$\nabla \cdot \boldsymbol{\sigma} + \mathbf{b} = \mathbf{0} \text{ in } \Omega \tag{20}$$

and

$$\begin{aligned} &\boldsymbol{\sigma} \cdot \mathbf{n} = \bar{\mathbf{t}} \quad \text{on } \Gamma_t \text{ (natural boundary conditions)} \\ &\mathbf{u} = \bar{\mathbf{u}} \quad \text{on } \Gamma_u \text{ (essential boundary conditions)} \end{aligned} \tag{21}$$

respectively, where $\boldsymbol{\sigma} = \mathbf{D}\boldsymbol{\epsilon}$ is the stress vector, $\mathbf{D}$ is the material property matrix, $\boldsymbol{\epsilon} = \nabla_s \mathbf{u}$ is the strain vector, $\mathbf{u}$ is the displacement vector, $\mathbf{b}$ is the body force vector, $\bar{\mathbf{t}}$ and $\bar{\mathbf{u}}$ are the vectors of prescribed surface tractions and displacements, respectively, $\mathbf{n}$ is a unit normal to domain, Ω, Γ_t and Γ_u are the portions of boundary, Γ where tractions and displacements are prescribed, respectively, $\nabla^{\mathrm{T}} = \{\partial/\partial x_1, \partial/\partial x_2\}$ is the vector of gradient operators, and $\nabla_s \mathbf{u}$ is the symmetric part of $\nabla \mathbf{u}$. The variational or weak form of Eqs. (20) and (21) is

$$\int_{\Omega} \boldsymbol{\sigma}^{\mathrm{T}} \delta\boldsymbol{\epsilon}\, d\Omega - \int_{\Omega} \mathbf{b}^{\mathrm{T}} \delta\mathbf{u}\, d\Omega - \int_{\Gamma_t} \bar{\mathbf{t}}^{\mathrm{T}} \delta\mathbf{u}\, d\Gamma - \delta W_u = 0 \tag{22}$$

where δ denotes the variation operator and δW_u represents a term to enforce the essential boundary conditions. The explicit form of this term depends on the method by which the essential boundary conditions are imposed [7]. In this study, W_u is defined as

$$W_u = \sum_{\mathbf{x}_J \in \Gamma_u} \mathbf{f}^{\mathrm{T}}(\mathbf{x}_J)[\mathbf{u}(\mathbf{x}_J) - \bar{\mathbf{u}}(\mathbf{x}_J)] \tag{23}$$

where $\mathbf{f}^{\mathrm{T}}(\mathbf{x}_J)$ is the vector of reaction forces at the constrained node $J \in \Gamma_u$. Hence,

$$\delta W_u = \sum_{\mathbf{x}_J \in \Gamma_u} \delta\mathbf{f}^{\mathrm{T}}(\mathbf{x}_J)[\mathbf{u}(\mathbf{x}_J) - \bar{\mathbf{u}}(\mathbf{x}_J)] + \mathbf{f}^{\mathrm{T}}(\mathbf{x}_J)\delta\mathbf{u}(\mathbf{x}_J) \tag{24}$$

Consider a single boundary constraint, $\bar{u}_i(\mathbf{x}_J) = g_i(\mathbf{x}_J)$ applied at node J in the direction of x_i coordinate. Then, the variational form given by Eqs. (22) and (24) can be expressed by

$$\int_\Omega \boldsymbol{\sigma}^{\mathrm{T}}\delta\boldsymbol{\epsilon}\, \mathrm{d}\Omega + f_i(\mathbf{x}_J)\delta u_i(\mathbf{x}_J) = \int_\Omega \mathbf{b}^{\mathrm{T}}\delta\mathbf{u}\, \mathrm{d}\Omega - \int_{\Gamma_t} \bar{\mathbf{t}}^{\mathrm{T}}\delta\mathbf{u}\, \mathrm{d}\Gamma \tag{25}$$

$$\delta f_i(\mathbf{x}_J)[u_i(\mathbf{x}_J) - g_i(\mathbf{x}_J)] = 0 \tag{26}$$

where $f_i(\mathbf{x}_J)$ and $u_i(\mathbf{x}_J)$ are the ith component of $f(\mathbf{x}_J)$ and $u(\mathbf{x}_J)$, respectively. From Eq. (11), the MLS approximation of $u_i(\mathbf{x}_J)$ is

$$u_i^h(\mathbf{x}_J) = \sum_{I=1}^{N} \Phi_I(\mathbf{x}_J) d_I^i = \boldsymbol{\Phi}_J^{i^{\mathrm{T}}} \mathbf{d} \tag{27}$$

where

$$\boldsymbol{\Phi}_J^{i^{\mathrm{T}}} = \begin{cases} \{\Phi_1(\mathbf{x}_J), 0, \Phi_2(\mathbf{x}_J), 0, \ldots, \Phi_N(\mathbf{x}_J), 0\}, & \text{when } i = 1 \\ \{0, \Phi_1(\mathbf{x}_J), 0, \Phi_2(\mathbf{x}_J), \ldots, 0, \Phi_N(\mathbf{x}_J)\}, & \text{when } i = 2 \end{cases} \tag{28}$$

$$\mathbf{d} = \begin{Bmatrix} d_1^1 \\ d_1^2 \\ d_2^1 \\ d_2^2 \\ \vdots \\ d_N^1 \\ d_N^2 \end{Bmatrix} \tag{29}$$

is the vector of nodal parameters or generalized displacements, and N is the total number of nodal points in Ω. Using Eqs. (27)–(29) into the discretization of Eqs. (25) and (26) gives [5–7]

$$\begin{bmatrix} \mathbf{k} & \boldsymbol{\Phi}_J^i \\ \boldsymbol{\Phi}_J^{i^{\mathrm{T}}} & 0 \end{bmatrix} \begin{Bmatrix} \mathbf{d} \\ f_i(\mathbf{x}_J) \end{Bmatrix} = \begin{Bmatrix} \mathbf{f}^{\mathrm{ext}} \\ g_i(\mathbf{x}_J) \end{Bmatrix} \tag{30}$$

where

$$\mathbf{k} = \begin{bmatrix} \mathbf{k}_{11} & \mathbf{k}_{12} & \ldots & \mathbf{k}_{1N} \\ \mathbf{k}_{21} & \mathbf{k}_{22} & \ldots & \mathbf{k}_{2N} \\ \vdots & \vdots & \vdots & \vdots \\ \mathbf{k}_{N1} & \mathbf{k}_{N2} & \ldots & \mathbf{k}_{NN} \end{bmatrix} \in \mathscr{L}(\Re^{2N} \times \Re^{2N}) \tag{31}$$

is the stiffness matrix with

$$\mathbf{k}_{IJ} = \int_\Omega \mathbf{B}_I^{\mathrm{T}} \mathbf{D} \mathbf{B}_J\, \mathrm{d}\Omega \in \mathscr{L}(\Re^2 \times \Re^2) \tag{32}$$

representing the contributions of Jth node at node I,

$$\mathbf{f}^{\mathrm{ext}} = \begin{Bmatrix} \mathbf{f}_1^{\mathrm{ext}} \\ \mathbf{f}_2^{\mathrm{ext}} \\ \vdots \\ \mathbf{f}_N^{\mathrm{ext}} \end{Bmatrix} \in \Re^{2N} \tag{33}$$

is the force vector with

$$\mathbf{f}_I^{\mathrm{ext}} = \int_\Omega \Phi_I \mathbf{b}^{\mathrm{T}}\, \mathrm{d}\Omega - \int_{\Gamma_t} \Phi_I \bar{\mathbf{t}}^{\mathrm{T}}\, \mathrm{d}\Gamma \in \Re^2 \ , \tag{34}$$

$$\mathbf{B}_I = \begin{bmatrix} \Phi_{I,1} & 0 \\ 0 & \Phi_{I,2} \\ \Phi_{I,2} & \Phi_{I,1} \end{bmatrix} \ , \tag{35}$$

and

$$\mathbf{D} = \begin{cases} \frac{E}{1-\nu^2} \begin{bmatrix} 1 & \nu & 0 \\ \nu & 1 & 0 \\ 0 & 0 & \frac{1-\nu}{2} \end{bmatrix}, & \text{for plane stress} \\ \frac{E}{(1+\nu)(1-2\nu)} \begin{bmatrix} 1-\nu & \nu & 0 \\ \nu & 1-\nu & 0 \\ 0 & 0 & \frac{1-2\nu}{2} \end{bmatrix}, & \text{for plane strain} \end{cases} \tag{36}$$

is the elasticity matrix with E and ν representing the elastic modulus and Poissons ratio, respectively.

In order to perform numerical integration in Eqs. (32) and (34), a background mesh is needed. This background mesh can be independent of the arrangement of meshless nodes. However, the nodes of the background mesh may coincide with the meshless nodes. Standard Gaussian quadrature was used to evaluate the integrals for assembling the stiffness matrix and the force vector. In general, a 3×3 quadrature is adequate, except in the cells surrounding the surrounding the crack tip where a 6×6 quadrature may be required [5].

5
Essential boundary conditions

Lack of Kronecker delta properties in the meshless shape functions, Φ_I poses some difficulties in imposing essential boundary conditions in EFGM. In this work, a full transformation method [22, 23], was used for fracture-mechanics applications.

Consider the transformation,

$$\hat{\mathbf{d}} = \boldsymbol{\Lambda}\mathbf{d} \tag{37}$$

where,

$$\hat{\mathbf{d}} = \begin{Bmatrix} u_1^h(\mathbf{x}_1) \\ u_2^h(\mathbf{x}_1) \\ u_1^h(\mathbf{x}_2) \\ u_2^h(\mathbf{x}_2) \\ \vdots \\ u_1^h(\mathbf{x}_N) \\ u_2^h(\mathbf{x}_N) \end{Bmatrix} \in \Re^{2N} \tag{38}$$

is the nodal displacement vector, and

$$\mathbf{\Lambda} = \begin{bmatrix} \mathbf{\Phi}_1^{1^{\mathrm{T}}} \\ \mathbf{\Phi}_1^{2^{\mathrm{T}}} \\ \mathbf{\Phi}_2^{1^{\mathrm{T}}} \\ \mathbf{\Phi}_2^{2^{\mathrm{T}}} \\ \vdots \\ \mathbf{\Phi}_N^{1^{\mathrm{T}}} \\ \mathbf{\Phi}_N^{2^{\mathrm{T}}} \end{bmatrix} \in \mathscr{L}(\Re^{2N} \times \Re^{2N}) \tag{39}$$

is the transformation matrix. Multiplying the first set of matrix equation in Eq. (30) by $\mathbf{\Lambda}^{-\mathrm{T}}$, one obtains

$$\begin{bmatrix} \Lambda^{-\mathrm{T}}\mathbf{k} & \mathbf{I}_J^i \\ \mathbf{\Phi}_J^{i^{\mathrm{T}}} & 0 \end{bmatrix} \begin{Bmatrix} \mathbf{d} \\ f_i(\mathbf{x}_J) \end{Bmatrix} = \begin{Bmatrix} \mathbf{\Lambda}^{-\mathrm{T}}\mathbf{f}^{\mathrm{ext}} \\ g_i(\mathbf{x}_J) \end{Bmatrix} \tag{40}$$

where

$$\mathbf{I}_J^i = \mathbf{\Lambda}^{-\mathrm{T}}\mathbf{\Phi}_J^i = \begin{Bmatrix} 0 \\ \vdots \\ 0 \\ 1 \\ 0 \\ \vdots \\ 0 \end{Bmatrix} \leftarrow [2(J-1)+i]\text{th row} \quad . \tag{41}$$

Let,

$$\hat{\mathbf{k}} = \begin{bmatrix} \hat{\mathbf{k}}_1^{\mathrm{T}} \\ \vdots \\ \hat{\mathbf{k}}_{2N}^{\mathrm{T}} \end{bmatrix} = \mathbf{\Lambda}^{-\mathrm{T}}\mathbf{k} \tag{42}$$

$$\hat{\mathbf{f}}^{\mathrm{ext}} = \mathbf{\Lambda}^{-\mathrm{T}}\mathbf{f}^{\mathrm{ext}} \tag{43}$$

where $\hat{\mathbf{k}}_i^{\mathrm{T}} = \{\hat{\mathbf{k}}_{i1}, \hat{\mathbf{k}}_{i2}, \ldots, \hat{\mathbf{k}}_{i(2N)}\}$, $i = 1, 2, \ldots, 2N$. Equation (40) can be re-written as

$$\begin{bmatrix} \hat{\mathbf{k}}_1^{\mathrm{T}} & 0 \\ \vdots & \vdots \\ \hat{\mathbf{k}}_{M-1}^{\mathrm{T}} & 0 \\ \hat{\mathbf{k}}_M^{\mathrm{T}} & 1 \\ \hat{\mathbf{k}}_{M+1}^{\mathrm{T}} & 0 \\ \vdots & \vdots \\ \hat{\mathbf{k}}_{2N}^{\mathrm{T}} & 0 \\ \mathbf{\Phi}_J^{i^{\mathrm{T}}} & 0 \end{bmatrix} \begin{Bmatrix} \mathbf{d} \\ f_i(\mathbf{x}_J) \end{Bmatrix} = \begin{Bmatrix} \hat{f}_1^{\mathrm{ext}} \\ \vdots \\ \hat{f}_{M-1}^{\mathrm{ext}} \\ \hat{f}_M^{\mathrm{ext}} \\ \hat{f}_{M+1}^{\mathrm{ext}} \\ \vdots \\ \hat{f}_{2N}^{\mathrm{ext}} \\ g_i(\mathbf{x}_J) \end{Bmatrix} \begin{matrix} \\ \\ \leftarrow [2(J-1)+i]\text{th row} \\ \\ \\ \\ \\ \leftarrow (2N+1)\text{th row} \end{matrix} \tag{44}$$

where $M = (2J-1)+i$. Exchanging the Mth and the last row of Eq. (44) leads to

$$\begin{bmatrix} \hat{\mathbf{k}}_1^{\mathrm{T}} & 0 \\ \vdots & \vdots \\ \hat{\mathbf{k}}_{M-1}^{\mathrm{T}} & 0 \\ \mathbf{\Phi}_J^{i^{\mathrm{T}}} & 0 \\ \hat{\mathbf{k}}_{M+1}^{\mathrm{T}} & 0 \\ \vdots & \vdots \\ \hat{\mathbf{k}}_{2N}^{\mathrm{T}} & 0 \\ \hat{\mathbf{k}}_M^{\mathrm{T}} & 1 \end{bmatrix} \begin{Bmatrix} \mathbf{d} \\ f_i(\mathbf{x}_J) \end{Bmatrix} = \begin{Bmatrix} \hat{f}_1^{\mathrm{ext}} \\ \vdots \\ \hat{f}_{M-1}^{\mathrm{ext}} \\ g_i(\mathbf{x}_J) \\ \hat{f}_{M+1}^{\mathrm{ext}} \\ \vdots \\ \hat{f}_{2N}^{\mathrm{ext}} \\ \hat{f}_M^{\mathrm{ext}} \end{Bmatrix} \begin{matrix} \\ \\ \leftarrow [2(J-1)+i]\text{th row} \\ \\ \\ \\ \\ \leftarrow (2N+1)\text{th row} \end{matrix} \tag{45}$$

which can be uncoupled as

$$\mathbf{K}\mathbf{d} = \mathbf{F} \tag{46}$$

$$\hat{\mathbf{k}}_M^{\mathrm{T}}\mathbf{d} + f_i(\mathbf{x}_J) = \hat{f}_M^{\mathrm{ext}} \tag{47}$$

where

$$\mathbf{K} = \mathscr{M}_J^i(\hat{\mathbf{k}}) = \begin{bmatrix} \hat{\mathbf{k}}_1^{\mathrm{T}} \\ \vdots \\ \hat{\mathbf{k}}_{M-1}^{\mathrm{T}} \\ \mathbf{\Phi}_J^{i^{\mathrm{T}}} \\ \hat{\mathbf{k}}_{M+1}^{\mathrm{T}} \\ \vdots \\ \vdots \\ \hat{\mathbf{k}}_{2N}^{\mathrm{T}} \end{bmatrix} \leftarrow [2(J-1)+i]\text{th row} \tag{48}$$

and

$$\mathbf{F} = \mathscr{N}_J^i(\hat{\mathbf{f}}^{\mathrm{ext}}) = \begin{Bmatrix} \hat{f}_1^{\mathrm{ext}} \\ \vdots \\ \hat{f}_{M-1}^{\mathrm{T}} \\ g_i(\mathbf{x}_J) \\ \hat{f}_{M+1}^{\mathrm{ext}} \\ \vdots \\ \vdots \\ \hat{f}_{2N}^{\mathrm{ext}} \end{Bmatrix} \leftarrow [2(J-1)+i]\text{th row} \tag{49}$$

are the modified stiffness matrix and force vectors respectively. Using Eq. (46), the generalized displacement vector, $\mathbf{d}$ can be solved efficiently without needing any Lagrange multipliers.

In Eqs. (48) and (49), $\mathscr{M}_J^i$ is a matrix operator that replaces the $[2(J-1)+i]$th row of $\hat{\mathbf{k}}$ by $\mathbf{\Phi}_J^{i^{\mathrm{T}}}$ and $\mathscr{N}_J^i$ is another matrix operator that replaces the $[2(J-1)+i]$th row of $\hat{\mathbf{f}}^{\mathrm{ext}}$ by $g_i(\mathbf{x}_J)$, due to the application of a single boundary constraint at node J. For multiple boundary constraints, similar operations can be repeated. Suppose, there are N_c number of essential boundary conditions at nodes, $J_1, J_2, \ldots, J_{N_c}$ applied in the directions, $i_1, i_2, \ldots, i_{N_c}$, respectively. Hence, the resulting modified stiffness matrix and force vector are

$$\mathbf{K} = \prod_{l=1}^{N_c} \mathscr{M}_{J_l}^{i_l}(\hat{\mathbf{k}}) \tag{50}$$

and

$$\mathbf{F} = \prod_{l=1}^{N_c} \mathscr{N}_{J_l}^{i_l}(\hat{\mathbf{f}}^{\text{ext}}) \ , \tag{51}$$

respectively.

6
Computational fracture mechanics

6.1
Calculation of stress-intensity factors

Consider a structure with a rectilinear crack of length, $2a$ that is subjected to external stresses. Let K_{I} and K_{II} be the stress-intensity factors (SIFs) for mode-I and mode-II, respectively. These SIFs can be evaluated using the interaction integral [24] converted into a domain form [25, 26]. For example,

$$K_{\text{I}} = \frac{E'}{2} M^{(1,2)} \tag{52}$$

where

$$E' = \begin{cases} E, & \text{plane stress} \\ \frac{E}{1-\nu^2}, & \text{plane strain} \end{cases} \tag{53}$$

is the effective elastic modulus, and $M^{(1,2)}$ is the interaction integral. It includes the terms from the actual mixed mode state for the given boundary conditions (superscript 1) and the super-imposed near-tip mode I auxiliary state (superscript 2). $M^{(1,2)}$ is given by

$$M^{(1,2)} = \int_A \left[\sigma_{ij}^{(1)} \frac{\partial u_i^{(2)}}{\partial x_1} + \sigma_{ij}^{(2)} \frac{\partial u_i^{(1)}}{\partial x_1} - W^{(1,2)} \delta_{1j} \right] \frac{\partial q}{\partial x_j} \, \mathrm{d}A \tag{54}$$

where σ_{ij} and u_i are the components of stress tensor and displacement vector, respectively, $W^{(1,2)}$ is the mutual strain energy from the two states and q is a weight function chosen such that it has a value of unity at the crack tip, zero along the boundary of the domain and arbitrary elsewhere. Note that all the quantities are evaluated with respect to a coordinate system with crack tip as origin. Following similar considerations, K_{II} can be calculated from Eqs. (52)–(54), except that the near-tip mode II state is chosen as auxiliary state while computing $M^{(1,2)}$.

6.2
Simulation of crack propagation

In order to simulate crack growth under linear-elastic condition, the crack-path direction must be determined. There are a number of criteria available to predict the direction of crack trajectory. They are based on: (1) maximum circumferential stress [27], (2) minimum strain energy density [28], (3) maximum energy release rate [29], and (4) vanishing in-plane SIF (K_{II}) in shear mode for infinitesimally small crack extension [30]. The first two criteria predict the direction of crack trajectory from the stress state prior to the crack extension. The last two criteria require stress analysis for virtually extended cracks in various directions to find the appropriate crack-growth directions. In this study, the crack-growth simulation was based on the first criterion only. Other criteria, which are not considered here, can be easily implemented into the proposed meshless method.

Crack trajectory prediction

According to the maximum circumferential stress criterion [27], the initial direction of crack propagation, θ, is the solution of the equation

$$K_{\text{I}} \sin\theta + K_{\text{II}}(3\cos\theta - 1) = 0 \ . \tag{55}$$

where K_{I} and K_{II} are SIFs for any instant during the crack growth. When the values of K_{I} and K_{II} are known, θ can be easily solved using standard numerical procedures.

Quasi-automatic crack propagation

A fully automatic strategy for crack propagation is the one which requires no user interaction to predict both the extent and direction of crack growth. The present approach is, however, quasi-automatic because the user still needs to provide a desired crack-length increment every time the crack tip moves. The quasi-automatic simulation of crack propagation involves a number of successive analyses. Each analysis consists of the following steps:

1. A meshless analysis is performed to predict stress and strain fields.
2. The SIFs are calculated from the results of step 1.
3. The direction of crack trajectory is calculated from Eq. (55).
4. For a user-defined crack-length increment, the location of the new crack-tip is determined. The crack geometry is updated.
5. The meshless node in the old crack-tip (if exists) is split into two nodes locating on the opposite sides of the crack.
6. New meshless nodes are added for improved discretization of the domain, if desired.

7
Numerical examples

The method developed in this study was applied to perform fracture-mechanics analysis of both stationary and propagating cracks. Both single- (mode I) and mixed-mode (modes I and II) conditions were considered and five examples are presented here. The value of $\lambda = 1$ was used in Examples 2 to 5. For numerical integration, a 6×6 Gauss quadrature rule was used in Example 1 and a 8×8 rule was used in all other examples for all cells of the background mesh.

7.1
Example 1: stationary crack under mode-I

Consider an edge-cracked plate under pure tension as shown in Fig. 1(a), that has length, $L = 2$ units, width, $W = 1$ units, and crack length, $a = 0.4$ units. The far-field tensile stress, $\sigma^{\infty} = 1$ units. Due to symmetry, only half of the plate was analyzed. An EFGM model consisting of 121

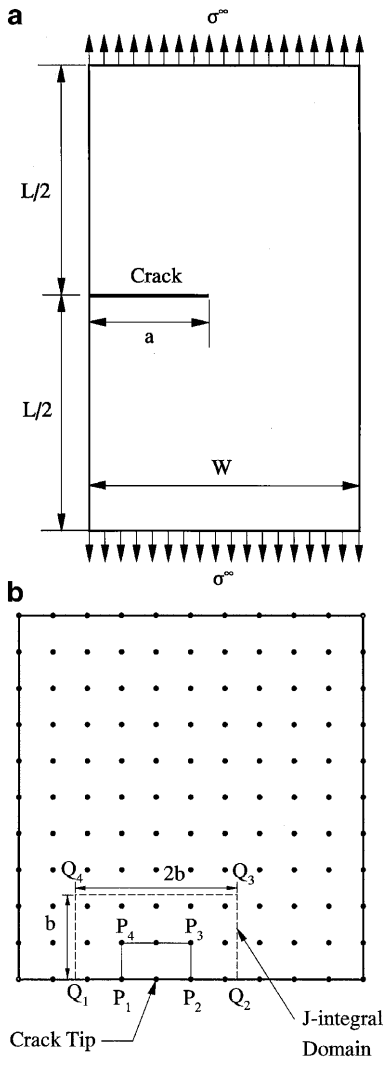

Fig. 1a, b. Edge-cracked plate under mode-I loading. **a** Geometry and loads; **b** meshless discretization (121 nodes)

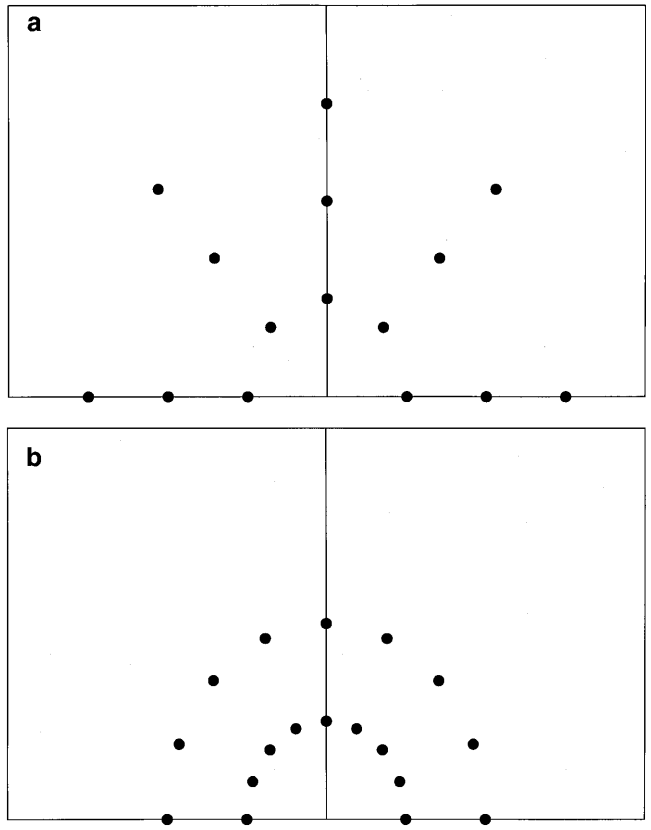

Fig. 2a, b. Nodal refinements at crack tip. **a** additional 15 nodes; **b** additional 18 nodes

uniformly spaced meshless nodes is shown in Fig. 1(b). The domain of the plate was divided by 10×10 rectangular cells with their nodes coincident with the meshless nodes solely for numerical integration. A domain $Q_1Q_2Q_3Q_4$ of size $2b \times b$ required for calculating the J-integral is defined in Fig. 1(b). Additional nodes of 15 and 18, shown in Fig. 2, were added in $P_1P_2P_3P_4$ [see Fig. 1(b)] to study the effect of crack-tip nodal refinement on SIF. A plane stress condition was assumed with $E = 207{,}000$ units and $\nu = 0.3$ units.

Table 1 shows the values of K_I for $N = 121$, 136 and 139 used in various nodal arrangements. A linear basis function and $\beta = 2$ was used for these calculations. For each nodal arrangement, the size of domain for J-integral calculation was 6.4×3.2 units. When compared with the benchmark solution of $K_I = 2.358$ units, given by Tada et al. [31], the predicted values of K_I from the present study are accurate. The accuracy improves with the increase of meshless nodes and refinement as expected. Table 2 also contains the EFGM results of SIF by Belytschko et al. [5] and Kaljevic and Saigal [15] calculated when $N = 121$ and 136. The reported results of K_I from the past do approach the reference solution, but their convergence rate is slightly lower than that in the present development. Further nodal refinements are needed to reach the accuracy of present results [5, 15]. No Lagrange multipliers or singular weight functions used by Belytschko et al. [5] and Kaljevic and Saigal [15] were needed or used in the present development.

Table 1. Mode-I stress-intensity factor using linear basis in various studies (Example 1)[a]

Nodal points (N)	Present study	Belytschko et al. [5]	Kaljevic and Saigal [13]
121	2.127 (0.901)	2.009 (0.852)	2.010 (0.853)
136	2.290 (0.971)	2.250 (0.954)	2.253 (0.956)
139	2.346 (0.995)	–[b]	–[b]

[a] Parenthetical values indicate the ratio of calculated SIF and the reference value of K_I = 2.358 units [27]
[b] Not calculated

Table 2. Mode-I stress-intensity factor using enriched basis functions (Example 1)[a]

Type of enrichment	K_I	SIF Ratio[a]
Full	2.366	1.003
Radial	2.360	1.001
Hybrid	2.337	0.991

[a] The SIF Ratio = Predicted SIF/Reference value of SIF, which is 2.358 units [27]

Table 2 presents results to study the effect of various basis functions on the calculation of SIF. Three basis functions involving full ($\beta = 4$), radial ($\beta = 5$), and hybrid ($\beta = 3$) enrichments were used to calculate K_I for the meshless discretization ($N = 121$) of Fig. 1(b) and the same J-integral domain of size 6.4×3.2 units. For the hybrid basis function, the fully enriched basis was used at the singularity-dominated region ($r/a \leq 0.1$) and linear basis at $r/a \geq 0.2$. The agreement between the predicted SIFs by the proposed method and reference solution is excellent. The use of enriched basis significantly improved the accuracy of SIF without needing further refinements at the crack tip.

Table 3. Mode-I stress-intensity factor using various integral domains (Example 1)[a]

Size of domain ($2b \times b$)	K_I	SIF Ratio[a]
1.6×0.8	2.361	1.001
3.2×1.6	2.357	0.999
4.8×2.4	2.358	1.000
6.4×3.2	2.366	1.003

[a] The SIF Ratio = Predicted SIF/Reference value of SIF. Reference value: K_I = 2.358 [27]

Finally, Table 3 shows the results of SIF for $N = 121$ using fully enriched basis function ($\beta = 4$) as a function of the size of J-integral domain. Very accurate results of SIF were obtained regardless of the size of the domain.

7.2
Example 2: near-tip mode-I stress field

In this example, the near-tip stress field of a square patch of size, $2a = 1$ units containing an edge crack of length, $a = 0.5$ units is investigated [Fig. 3(a)]. The distributions of the patch with 175 meshless nodes are shown in Fig. 3(b). The linear-elastic displacement field corresponding to a pure mode-I SIF value of $K_I = 1$ units was applied along the outer boundary of the patch. The objective is to predict the near-tip stress field by the meshless method and compare with the corresponding LEFM singularity field. A plane stress condition was assumed with the same values of E and v in Example 1.

Using a fully enriched basis and $\beta = 4$, Fig. 4 shows the plots of radial (σ_{rr}) and circumferential ($\sigma_{\theta\theta}$) stresses as a function of r/a, when $\theta = 0$. For $r = 0.1a$, the angular variations of σ_{rr}, $\sigma_{\theta\theta}$, and shear stress, $\tau_{r\theta}$, are also shown in Fig. 5. Figures 4 and 5 also include the plots of exact stresses from the LEFM singularity field. The predicted stresses from the meshless method match very well with the exact stresses. Similar accuracy of stresses was also

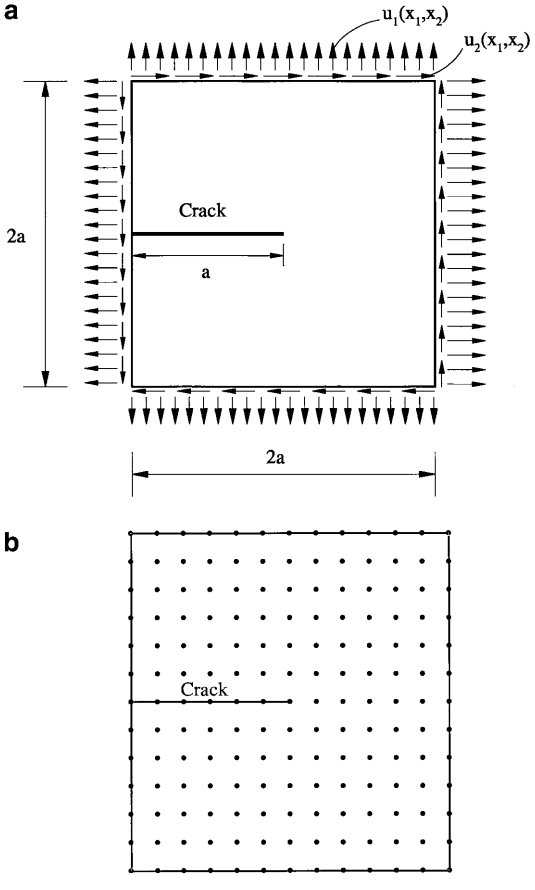

Fig. 3a, b. A square patch subjected to mode-I displacement field. **a** Geometry and applied displacements; **b** meshless discretization (175 nodes)

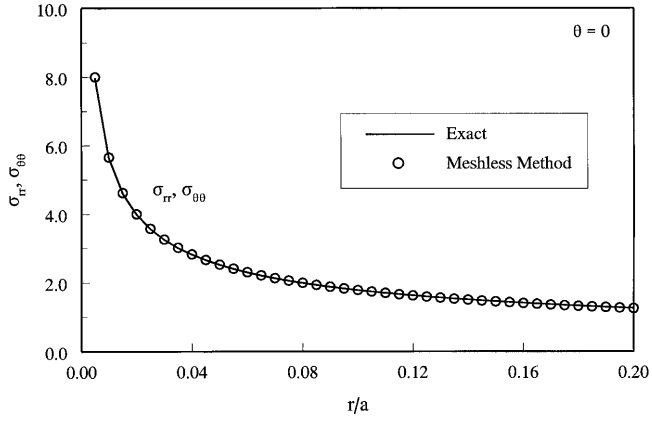

Fig. 4. Near-tip stress field ahead of crack tip

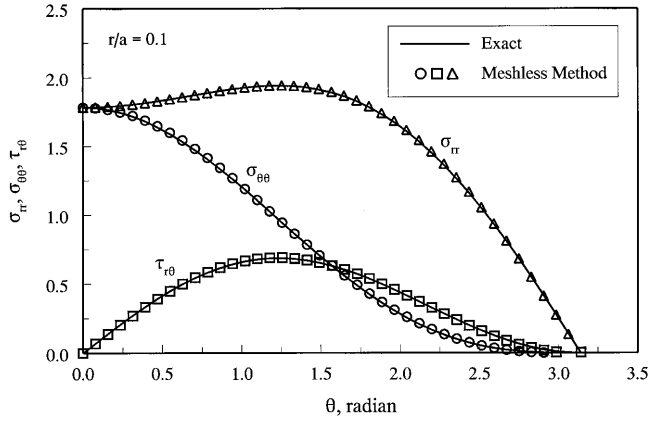

Fig. 5. Angular variation of stresses for $r/a = 0.1$

demonstrated by Fleming et al. [19] using a modified variational approach. The results of this study, however, were obtained using the original variational equation and the transformation method for boundary conditions.

7.3
Example 3: stationary crack under mixed-mode

This example involves an edge-cracked plate in Fig. 6(a), which is fixed at the bottom and subjected to far-field shear stress, $\tau^{\infty} = 1$ unit applied on the top. The plate has length, $L = 16$ units, width, $W = 7$ units, and crack length, $a = 3.5$ units. A domain of size $2b_1 \times 2b_2$ required for calculating the $M^{(1,2)}$ integral is also shown in Fig. 6(a). Figure 6(b) shows the meshless discretization involving 324 uniformly spaced nodes. A background mesh with cell points coincident with the meshless nodes was used. The elastic modulus and Poissons ratio were 30×10^6 units and 0.25, respectively. A plane strain condition was assumed. The mode-I and mode-II SIFs were calculated according to Eqs. (52)–(54).

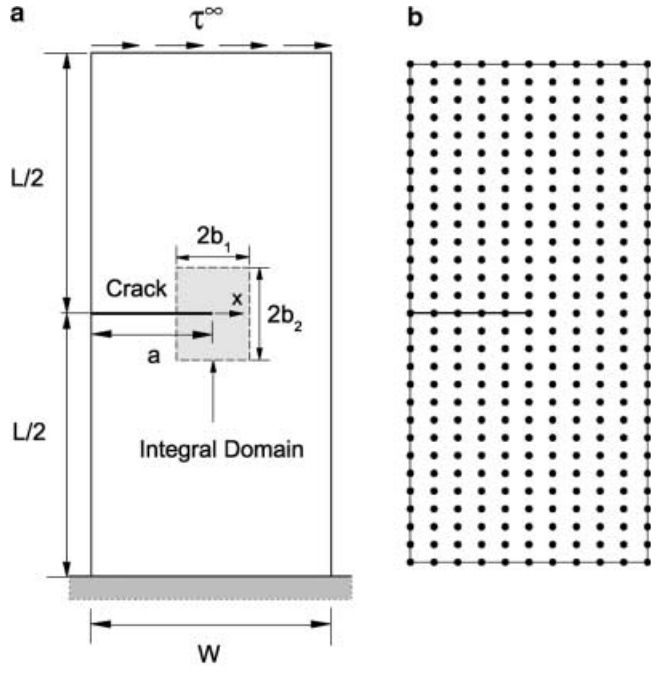

Fig. 6a, b. Edge-cracked plate under mixed-mode loading. **a** Geometry, loads, and domain size; **b** meshless discretization (324 nodes)

Table 4. Mixed-mode stress-intensity factor using various integral domains (Example 3)[a]

Size of domain ($2b_1 \times 2b_2$)	Mode-I		Mode-II	
	K_I	SIF Ratio	K_{II}	SIF Ratio
2.8×4.0	33.38	0.982	4.578	1.006
5.6×6.0	33.62	0.989	4.545	0.999
5.6×10.0	33.65	0.990	4.547	0.999
7.0×10.0	33.67	0.990	4.540	0.998
7.0×12.0	33.67	0.990	4.540	0.998
7.0×16.0	33.68	0.991	4.541	0.998

[a] SIF Ratio = Predicted SIF/reference value of SIF. Reference values: $K_I = 34.0$ units and $K_{II} = 4.55$ units [32]

Table 4 shows the predicted K_I and K_{II} for this edge-cracked problem using a fully enriched basis function, ($\beta = 4$), and various sizes of fracture integral domain. No major effects of domain size are seen. The reference solutions for this problem are: $K_I = 34.0$ units and $K_{II} = 4.55$ units [32]. They compare very well with the calculated SIFs given in Table 4. Similar results were reported by Fleming et al. [19].

7.4
Example 4: propagating crack under mixed-mode

Consider the edge-crack problem of Example 3. In this example, the accuracy of crack-path prediction using meshless method is evaluated. A fully enriched basis function was used. A domain size with $2b_1 = 2b_2 = 0.45$ units surrounding the crack tip was chosen for evaluating the $M^{(1,2)}$ integral. For the initial crack, the orientation of this domain is as shown in the Fig. 6(a). When the crack tip moves, the domain also moves in such a way that its center and local x-axis coincide with the new crack tip and direction of crack propagation, respectively. Otherwise, all other meshless input parameters are the same as in Example 3. For crack-propagation analysis, the maximum circumferential stress criterion was used.

Figure 7 shows the evolution of crack trajectory using the proposed method. The increment of crack length during each step of crack propagation was 4% of the initial crack length. At each increment, a new node was added at the crack tip. For comparison, a similar crack-growth analysis was performed using the FEM. The FEM involves quarter-point singularity elements and an automatic remeshing procedure for updating crack-tip mesh during the progression of crack growth. The predicted crack path from the meshless method almost coincides with the crack path from FEM. A similar accuracy of the crack trajectory is maintained without the burdensome remeshing required by FEM. Hence, the complexity of crack-propagation analysis can be significantly reduced by using the meshless method.

7.5
Example 5: experimental validation

In this example, crack trajectories predicted by the proposed method are compared with the Pustejovsky's

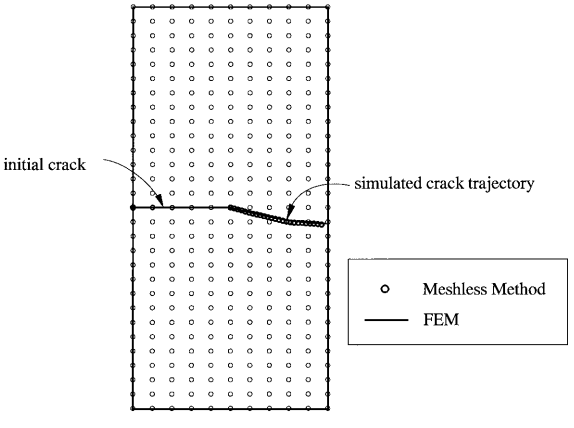

Fig. 7. Simulation of crack propagation by meshless and finite element methods

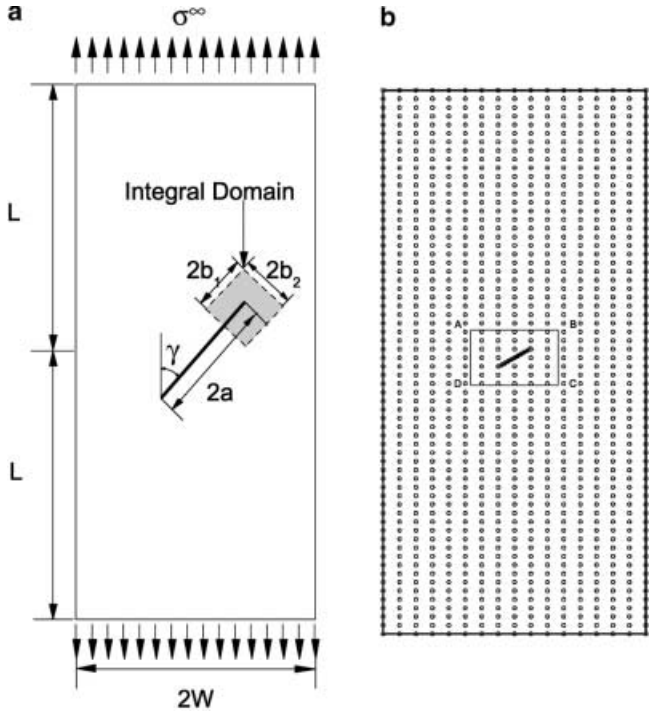

Fig. 8a, b. Center-oblique-cracked titanium Ti-6Al-4V plate under uniaxial loading. **a** Geometry, loads, and domain size; **b** Meshless discretization (1124 nodes)

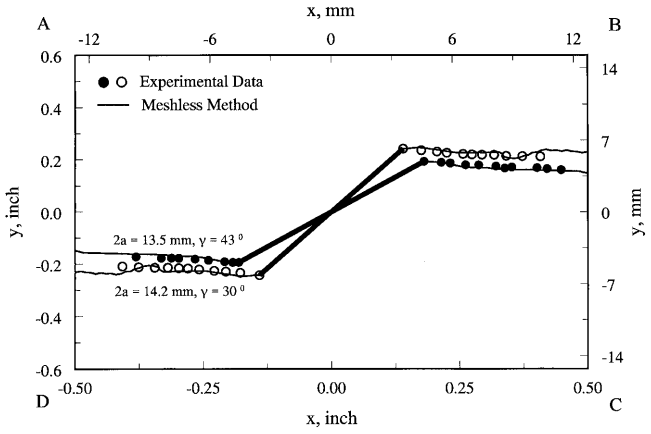

Fig. 9. Comparison of simulated crack trajectory by meshless with experimental data

experimental data [33, 34]. Pustejovsky performed a series of uniaxial tension tests on isotropic Titanium Ti-6Al-4V plates with oblique center-cracks of length $2a = 13.5$ mm (0.53 inch) at $\gamma = 43^\circ$ and length $2a = 14.2$ mm (0.56 inch) at $\gamma = 30^\circ$. The reported dimensions and material properties of the specimens were: length, $2L = 304.8$ mm (12 inches), width, $2W = 76.2$ mm (3 inches), elastic modulus, $E = 110$ GPa (16,000 ksi) and Poissons ratio, $\nu = 0.29$. A far-field uniaxial tensile stress, $\sigma^\infty = 207$ MPa (30 ksi) was applied on the top and the bottom of the specimen during meshless analysis. Figure 8(a) and (b) show the dimensions of the specimen and the meshless discretization, respectively. A hybrid enrichment of basis function was adopted by using fully enriched basis function for a small region close to the two crack tip regions and by using linear basis function for the rest of the domain. The inner radius of the coupling region for hybrid enrichment was $0.5a$ and the outer radius was $0.75a$. As shown in the Fig. 8(a), a domain size with $2b_1 = 2b_2 = 1.6$ mm (0.0625 inch) surrounding the crack tip was chosen for evaluating the $M^{(1,2)}$ integral for the initial crack. During crack propagation, the domain was moved the same way as explained in Example 4. A plane strain condition was assumed during the analysis.

Figure 9 shows the comparison of the predicted crack trajectories by the proposed meshless method with the experimental data in a small region *ABCD* [see Fig. 8(b)] surrounding the crack. The results of both cracks, one with $2a = 13.5$ mm (0.53 inch) and $\gamma = 43^\circ$ and the other with $2a = 14.2$ mm (0.56 inch) and $\gamma = 30^\circ$, are shown in Fig. 9. In both cases, the increment of crack length at each crack tip during each step of crack propagation was 2% of the initial crack length. The predicted crack trajectories are in good agreement with the experimental results.

8
Summary and conclusions

An efficient meshless method was developed to analyze linear-elastic cracked structures subject to single- or mixed-mode loading conditions. The method involves an element-free Galerkin formulation in conjunction with an exact implementation of essential boundary conditions and a new weight function. The proposed method eliminates the shortcomings of Lagrange multipliers commonly used in element-free Galerkin formulations. Numerical examples show that the proposed method yields accurate estimates of stress-intensity factors and near-tip stress field for two-dimensional cracked structures. Furthermore, this method was applied to model crack propagation under mixed-mode condition. Since the method is meshless, a structured mesh is not required; only a scattered set of nodal points is needed in the domain of interest. Since no element connectivity data are needed, the burdensome remeshing required by the finite element method is avoided. By sidestepping remeshing requirement, crack-propagation analysis can be dramatically simplified. Example problems on mixed-mode condition show that the predicted crack trajectories by the proposed meshless method are in excellent agreement with the finite element results or the experimental data.

References

1. **Lucy L** (1977) A numerical approach to testing the fission hypothesis. Astron. J. 82: 1013–1024
2. **Monaghan JJ** (1988) An introduction to SPH. Comp. Phys. Commun. 48: 89–96
3. **Libersky LD, Petschek AG, Carney TC, Hipp JR, Alliahdadi FZ** (1993) High strain Lagrangian hydrodynamics. J. Comp. Phys. 109: 67–75
4. **Nayroles B, Touzot G, Villon P** (1992) Generalizing the finite element method: diffuse approximation and diffuse elements. Comp. Mech. 10: 307–318
5. **Belytschko T, Lu YY, Gu L** (1994) Element-free Galerkin methods. Int. J. Numer. Meth. Engng 37: 229–256

6. **Lu YY, Belytschko T, Gu L** (1994) A new implementation of the element free Galerkin method. Comp. Meth. Appl. Mech. Engng 113: 397–414
7. **Belytschko T, Lu YY, Gu L** (1995) Crack propagation by element-free Galerkin methods. Engng Frac. Mech. 51(2): 295–315
8. **Duarte CAM, Oden JT** (1996) H-p clouds – an h-p meshless method. Numer. Meth. Part. Differ. Eqn 12(6): 673–705
9. **Melenk JM, Babuska I** (1996) The partition of unity finite element method: basic theory and applications. Comp. Meth. Appl. Mech. Engng 139: 280–314
10. **Liu WK, Jun S, Zhang YF** (1995) Reproducing kernel particle methods. Int. J. Numer. Meth. Fluids 20: 1081–1106
11. **Liu WK, Li S, Belytschko T** (1997) Moving least square Kernel Galerkin method – Part I: Methodology and convergence. Comp. Meth. Appl. Mech. Engng 143: 422–433
12. **Atluri SN, Zhu T** (1998) A new meshless local Petrov-Galerkin (MLPG) approach in computational mechanics. Comp. Mech. 22: 117–127
13. **Atluri SN, Sladek J, Sladek V, Zhu T** (2000) The local boundary integral equation (LBIE) and it's meshless implementation for linear elasticity. Comp. Mech. 25: 180–198
14. **Krongauz Y, Belytschko T** (1996) Enforcement of essential boundary conditions in meshless approximation using finite elements. Comp. Meth. Appl. Mech. Engng 131: 1335–1345
15. **Kaljevic I, Saigal S** (1997) An improved element free Galerkin formulation. Int. J. Numer. Meth. Engng 40: 2953–2974
16. **Zhu T, Atluri SN** (1998) A modified collocation method and a penalty formulation for enforcing the essential boundary conditions in the element free Galerkin method. Comp. Mech. 21: 211–222
17. **Mukherjee YX, Mukherjee S** (1997) On boundary conditions in the element-free Galerkin method. Comp. Mech. 19: 264–270
18. **Lancaster P, Salkauskas K** (1981) Surfaces generated by moving least squares methods. Math. Comp. 37: 141–158
19. **Fleming M, Chu YA, Moran B, Belytschko T, Lu YY, Gu L** (1997) Enriched element-free Galerkin methods for crack-tip fields. Int. J. Numer. Meth. Engng 40: 1483–1504
20. **Middleton D** (1996) An Introduction to Statistical Communication Theory. IEEE Press, Piscataway, NJ
21. **Organ DJ, Fleming M, Terry T, Belytschko T** (1996) Continuous meshless approximations for non-convex bodies by diffraction and transparency. Comp. Mech. 18: 225–235
22. **Atluri SN, Kim HG, Cho JY** (1999) A critical assessment of the truly meshless local Petrov-Galerkin (MLPG), and local boundary integral equation (LBIE) methods. Comp. Mech. 24: 348–372
23. **Chen JS, Wang HP** (2000) New boundary condition treatments in meshfree computation of contact problems. Comp. Meth. Appl. Mech. Engng 187(3–4): 441–468
24. **Yau JF, Wang SS, Corten HT** (1980) A mixed-mode crack analysis of isotropic solids using conservation laws of elasticity. J. Appl. Mech. 47: 335–341
25. **Moran B, Shih F** (1987) Crack tip and associated domain integrals from momentum and energy balance. Engng Fract. Mech. 27: 615–642
26. **Nikishkov GP, Atluri SN** (1987) Calculation of fracture mechanics parameters for an arbitrary 3-dimensional crack by the equivalent domain integral method. Int. J. Numer. Meth. Engng 24: 1801–1821
27. **Erdogan F, Sih GC** (1963) On the crack extension in plates under plane loading and transverse shear. J. Basic Engng 85: 519–527
28. **Sih GC** (1974) Strain-energy-density factor applied to mixed-mode crack problems. Int. J. Fract. 10: 305–321
29. **Wu CH** (1978) Fracture under combined loads by maximum energy release rate criterion. J. Appl. Mech. 45: 553–558
30. **Goldstein RV, Salganik RL** (1974) Brittle fracture of solids with arbitrary cracks. Int. J. Fract. 10: 507–527
31. **Tada H, Paris PC, Irwin GR** (1973) The Stress Analysis of Cracks Handbook. Del Research Corporation, Hellertown, PA
32. **Wilson WK** (1969) Combined mode fracture mechanics. Ph.D. Thesis, University of Pittsburgh, PA
33. **Pustejovsky MA** (1979a) Fatigue crack propagation in titanium under general in-plane loading – I: Experiments. Engng Frac. Mech. 11: 9–15
34. **Pustejovsky MA** (1979b) Fatigue crack propagation in titanium under general in-plane loading – II: Analysis Engng Frac. Mech. 11: 17–31